Stable near-to-ideal performance of a solution-grown single-crystal perovskite X-ray detector

Maksym Kovalenko (✉ mvkovalenko@ethz.ch)

  Swiss Federal Institute of Technology in Zurich   https://orcid.org/0000-0002-6396-8938

Kostiantyn Sakhatskyi

  ETH Zurich

Bekir Turedi

  KAUST

Gebhard Matt

  ETH Zurich

Muhammad Lintangpradipto

  KAUST

Rounak Naphade

  KAUST

Omar Mohammed

  King Abdullah University of Science and Technology   https://orcid.org/0000-0001-8500-1130

Sergii Yakunin

  ETH Zurich

Osman Bakr

  King Abdullah University of Science and Technology   https://orcid.org/0000-0002-3428-1002

Stable near-to-ideal performance of a solution-grown single-crystal perovskite X-ray detector

Kostiantyn Sakhatskyi[1,2,5], Bekir Turedi[3,5], Gebhard J. Matt[1,2], Muhammad Naufal Lintangpradipto[3], Rounak Naphade[3], Omar F. Mohammed[3,4], Sergii Yakunin[*1,2], Osman M. Bakr[*3], Maksym V. Kovalenko[*1,2]

[1] Laboratory of Inorganic Chemistry, Department of Chemistry and Applied Biosciences, ETH Zürich, CH-8093 Zürich, Switzerland

[2] Laboratory for Thin Films and Photovoltaics, Empa – Swiss Federal Laboratories for Materials Science and Technology, CH-8600 Dübendorf, Switzerland

[3] KAUST Catalysis Center (KCC), Division of Physical Sciences and Engineering, King Abdullah University of Science and Technology (KAUST), Thuwal 23955-6900, Kingdom of Saudi Arabia

[4] Advanced Membranes and Porous Materials Center, Division of Physical Science and Engineering, King Abdullah University of Science and Technology, Thuwal 23955-6900, Kingdom of Saudi Arabia

[5] These authors contributed equally: Kostiantyn Sakhatskyi and Bekir Turedi.

[*]E-mail: mvkovalenko@ethz.ch; osman.bakr@kaust.edu.sa; yakunins@ethz.ch

The ideal photodetector is the one able to detect every single incoming photon. In particular, in X-ray medical imaging, the radiation dose for patients can then approach its fundamentally lowest limit set by the Poisson photon statistics. Such near-to-ideal X-ray detection characteristics have been demonstrated with only a few semiconductor materials such as Si[1] and CdTe[2]; however, their industrial deployment in medical diagnostics is still impeded by elaborate and costly fabrication processes. Hybrid metal halide perovskites – newcomer semiconductors -– make for a viable alternative[3,4,5] owing to their scalable, inexpensive, robust, and versatile solution growth and recent demonstrations of single gamma-photon counting under high applied bias voltages[6,7]. The major hurdle with perovskites as mixed electronic-ionic conductors, however, arises from the rapid material's degradation under high electric field[8,9,10,11], thus far used in perovskite X-ray detectors[12,13]. Here we show that both near-to-ideal and long-term stable performance of perovskite X-ray detectors can be attained in the photovoltaic mode of operation at zero-voltage bias, employing thick and uniform methylammonium lead iodide (MAPbI$_3$) single crystal (SC) films (up to 300 μm), solution-grown directly on hole-transporting electrodes. The operational device stability is equivalent to the intrinsic chemical shelf lifetime of MAPbI$_3$, being at least one year in the studied case. Detection efficiency of 88% and noise equivalent dose of 90 pGy$_{air}$ (lower than the dose of a single incident photon) are obtained with 18 keV X-rays, allowing for single-photon counting, as well as low-dose and energy-resolved X-ray imaging. These findings benchmark hybrid perovskites as practically suited materials for developing low-cost commercial detector arrays for X-ray imaging technologies.

For a semiconductor to serve as an X-ray detector with characteristics approaching ideal performance, several requirements must be fulfilled: high resistivity ($\leq 10^{10}$ Ω cm) and hence sufficiently low noise levels for resolving charges generated by a single photon, high carrier mobility-lifetime ($\mu\tau$) product for the efficient collection of photon-generated carriers, and absorption of (nearly) all X-ray photons—the latter scales with the thickness and the average atomic number (Z) of constituting elements. Very few high-Z semiconductors were proposed to fulfill these requirements at room temperature[6,14,15,16,17] and thus far, only costly, ultrapure CdTe and CdZnTe single crystals, usually grown from a melt by high-pressure Bridgman or by Czochralski methods, have been commercially deployed[18,19]. Lead halide perovskite semiconductors (general formula $APbX_3$, where A is a cation, either organic methylammonium (MA^+) or formamidinium, or inorganic Cs^+; and X is an anion of I, Br or Cl halogen) are the most intensely studied class of contender high-Z materials for high-energy photon detection[3,4,5,6,7,12,13,20,21,22,23,24,25,26,27,28]. Excellent electronic characteristics are commonplace with both inexpensive solution-growth techniques (for all A-cations)[6,7,28] and with the melt-growth ($CsPbBr_3$ or $CsPbCl_3$)[26,29], often using conventional purity of precursors. Calculated X-ray absorption coefficients are even a few-fold higher compared to CdTe for soft X-rays (Extended Data Fig. 1).

We find that the major question, pertaining to the eventual utility of perovskites as commercial X-ray detectors, is the demonstration of simultaneously stable operation and near-ideal characteristics of such devices. Even for such high-Z and high-$\mu\tau$ materials as CdTe and $APbI_3$ perovskites, the required collection of photocarriers requires high voltages of hundreds-to-thousands volts applied across mm-to-cm materials thicknesses (depending upon the detected photons energies, which range from tens to hundreds of keV). The long-term operational stability is limited mainly by the stability of the semiconductor and interfaces under such high electric bias. The issue is especially acute for perovskites, as they are mixed electronic-ionic conductors, in which high dark currents and unstable performance often arise from the ion migration or electromigration of the contact materials, as well as electrochemical damage to the active material[8,9,10,11].

We consider the problem of high-bias stability of perovskites as inherently insurmountable, necessitating the research into low-voltage device concepts. In this work, we focus on using a photovoltaic device, wherein the only electric field is the one originating from the work-function asymmetry of the used electrical contacts. This notion is supported by the recent advancements in the long-term operational stability of perovskite solar cells[30]. Considering the high calculated value of the soft X-ray linear absorption coefficient of $MAPbI_3$ (Extended Data Fig. 1), taking the highest reported $\mu\tau$ values for this material (up to 10^{-2} cm^2 V^{-1}), and a typical build-in potential of one volt, we estimate that the requirement of simultaneously high charge-collection efficiency (CCE) close to

unity along with near-complete X-ray absorption (10-30 keV) can be met by a active layer having a thickness in the range of 50-500 µm. The practical embodiment of such an X-ray photovoltaic (XPV) device is essentially a highly efficient perovskite solar cell with a single-crystalline (SC) absorption layer of several hundred µm. Utilization of polycrystalline thick perovskite layers is unacceptable owing to orders-of-magnitude lower $\mu\tau$-values due to carrier scattering at the grain boundaries and defects[31,32], which proportionally compromises the CCE values and necessitates higher applied bias.

Motivated by the recent advances in the solution-growth of highly efficient SC perovskite solar cells ($\sim$20 µm[33,34,35]), we sought to obtain several-hundred-µm thick perovskite $MAPbI_3$ SC XPV devices (Fig. 1a, b). Such an order-of-magnitude thicker SC layer was grown directly on a conductive substrate by a low-temperature solution method. While operating in the XPV mode (*e.g.* zero applied bias), the devices exhibit near-to-ideal performance, which includes noise-equivalent dose below one X-ray photon and detection efficiency close to unity. These characteristics are retained for at least a year. X-ray imaging at extremely low doses at the tens of nGy_{air} level is obtained as well. Furthermore, energy-resolved X-ray imaging could be demonstrated, discriminating between materials of different compositions, which are otherwise indistinguishable in contrast-only X-ray transmission imaging.

$MAPbI_3$ SC XPV devices.

For obtaining a few hundred micrometers thick $MAPbI_3$ SC films, a space-confined inverse temperature crystallization method was adopted and adjusted from Ref[33,36]. The perovskite films were grown on indium tin oxide (ITO) substrates coated with poly(triaryl)amine (PTAA) as a hole-transporting layer, followed by the thermal evaporation of C_{60}/bathocuproine (BCP) layers as the electron-transporting layer and Cu electrode, completing the XPV device (Fig. 1a-c). Contacts with asymmetric work function potentials for establishing an internal electrical field and good charge selectivity of the transport layers are paramount for desired XPV operation mode. Nevertheless, the as-obtained thick XPV devices had poor detector performance, which we attribute to the effect of persistent, residual solvates that may form with the specific solvent used (γ-butyrolactone)[37]. The issue was satisfactorily mitigated with the extensive post-drying of crystals at room temperature in a nitrogen-filled drybox. Supplementary Fig. 1 illustrates the improvement of the X-ray detection performance (expressed in normalized signal-to-noise ratio (SNR) under the same dose rate) with post-conditioning time, which is correlated with the decrease of shunt conductivity and the rise of the X-ray photocurrent. SNR value reaches a saturated value typically in *ca.* one month.
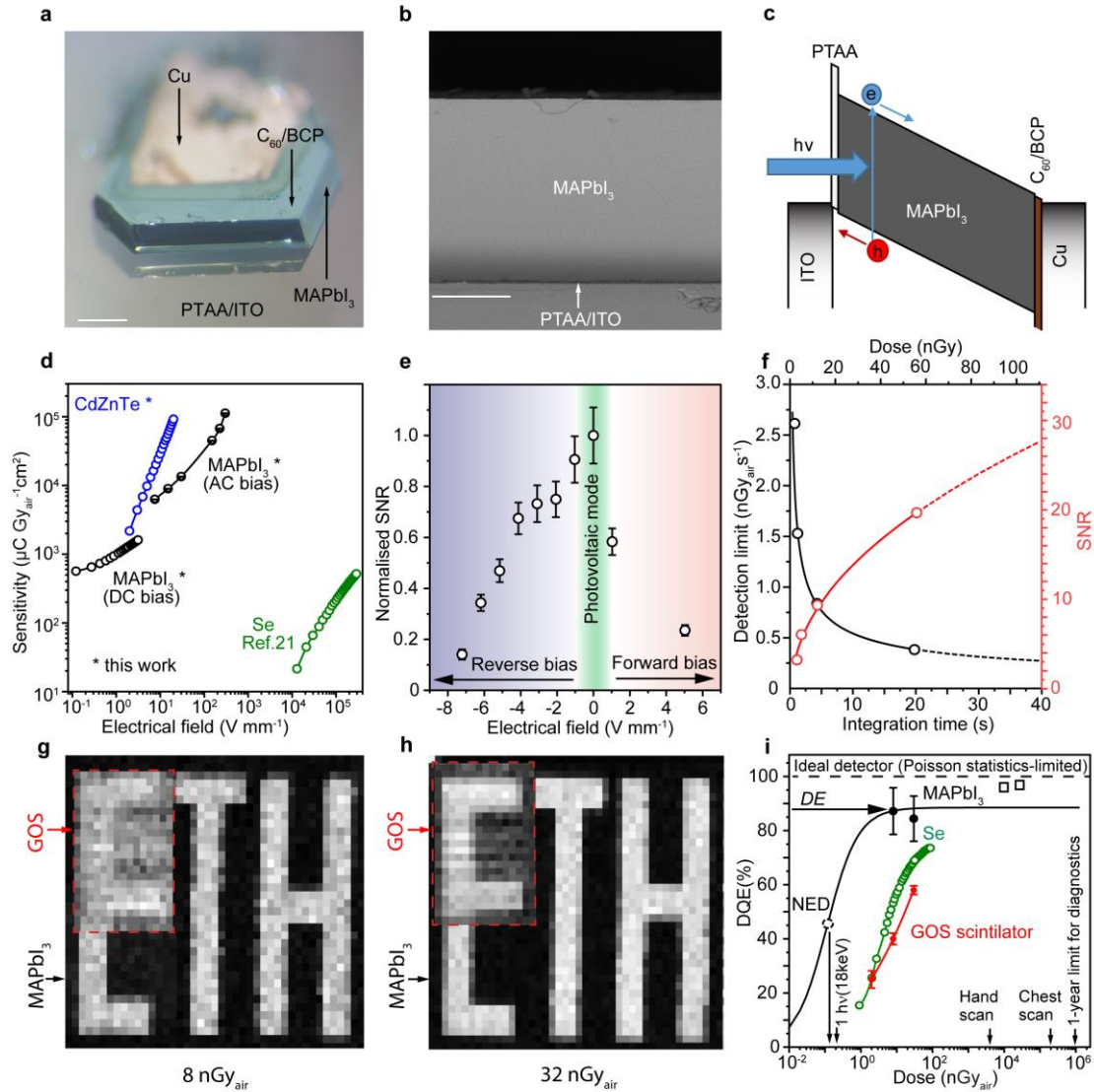
Fig. 1 | MAPbI₃ SC X-ray detector and its figures-of-merit. a, 110 µm MAPbI$_3$ SC XPV device with the description of layers. The scale bar is 200 µm. **b**, Cross-sectional scanning electron microscope image of a MAPbI$_3$ SC grown directly on PTAA/ITO substrate. The scale bar is 50 µm. **c**, Energy band alignment and operation principle in XPV mode. **d,** X-ray sensitivity dependence on the electric field for different materials. **e,** SNR degradation with the applied external electric field for a MAPbI$_3$ SC detector under constant X-ray irradiation. **f,** Decrease of DL and increase of SNR at longer integration times come at the cost of a high dose, for a MAPbI$_3$ SC XPV detector under X-ray irradiation. **g**, **h**, X-ray imaging of stencil mask (Supplementary Fig. 2) at doses of 8 nGy$_{air}$ (**d**) and 32 nGy$_{air}$ (**e**). Insets show imaging with the GOS scintillator detector. **i,** DQE dependencies on the dose. The solid black line and points represent, respectively, model and experimental data (calculated from **g** and **h**) for a MAPbI$_3$ SC. Red points are experimental data for the GOS scintillator. Green points are amorphous Se data from Ref.[21]. Black open squares show calculated DQE for doses, at which X-ray imaging was previously demonstrated with MAPbI$_3$ detectors[25,13].

Figures-of-merit and ideality of perovskite X-ray detectors. Performance characteristics that are most relevant practically and can objectively compare perovskite detectors across the laboratories need to be discussed first. X-ray sensitivity is by far the most commonplace reported figure-of-merit in the rapidly growing area of perovskite X-ray detectors, owing to the simplicity of its measurement. Higher sensitivities are achieved by device biasing at higher electrical fields and hence at the cost of excessive noise and dramatic degradation of the signal-to-noise ratio (Fig. 1d, e). Unlike conventional semiconductors such as CdTe, lead halide perovskites are mixed electronic-ionic conductors [38], further magnifying the electronic and electrochemical instabilities at high bias. Furthermore, emphasizing sensitivity may erroneously motivate research efforts towards photoconductors, as in the latter the sensitivity can be amplified *via* photoconductive gain[39]. The latter, however, accordingly also increases the noise levels, response time and device instability. This approach is of somewhat limited utility for the materials with poor charge transport characteristics (i.e. a-Se, QDs, *etc.*) and, in the case of perovskites, would require imparting imbalanced charge transport by, for instance, intentional deterioration of the material by introducing charge traps.

Another characteristic, commonly used for perovskite detectors is the detection limit (DL) of the dose rate[24,20,40], which remains a highly ambiguous parameter as it scales with the integration time (Fig. 1f). As the resulting DL is lower for a higher accumulated dose, the utility of reported DL values is higher when the integration times are specified (see details in Supplementary Notes 1-3). An overarching objective, foremost in medical imaging, is to attain the desired imaging performance at the lowest acquired radiation dose. In this regard, $MAPbI_3$ SC detector operated in XPV-mode (0V-bias) compares favorably with the state-of-the-art commercial scintillator gadolinium oxysulfide (GOS) detectors in terms of image contrast and image noise, especially when decreasing the dose to as low as 8 nGy_{air} (Fig. 1g, h). Quantitatively, the image quality is determined by the SNR, which for the ideal detector has the fundamental limit given by Poisson statistics - the photon shot noise. Denoting n_{ph} as the mean number of X-ray photons incident to the detector, the limit for SNR is $SNR_{ideal} = \sqrt{n_{ph}}$[41]. Consequently, a well-thought figure-of-merit is the Detective Quantum Efficiency (DQE) defined *via* SNR analysis as $DQE = SNR(D)_{detector}^2 / SNR(D)_{ideal}^2$ as a function of the incident dose D[42]. The DQE is commonly used for benchmarking commercial X-ray imagers, regardless of the detector technology (*i.e.* scintillating or direct detection). To represent the DQE as a function of D (*i.e.* $\propto n_{ph}$), we propose the following model for a single-pixel device:

$$DQE\,(D) = \frac{DE}{1 + \dfrac{NED}{D}}; \tag{1}$$

where NED is the Noise Equivalent Dose[43] and DE is the Detection Efficiency [see Supplementary Note 1 for the derivation of Eq. (1)]. DE is the fraction of detected photons *vs.* total incoming photons, which is given by an integral for a product of Attenuation Efficiency (AE) and CCE over the detector thickness. The NED is such a dose $D(n_{ph})$ for which the photon shot noise is equal to the intrinsic electric detector noise (DN), the latter comprising thermal noise, charge carrier shot noise, *etc.*

The ideal detector has DE of unity and a NED $<<$ D of a single photon and hence dose-independent DQE approaching unity. The dose can thus be minimized to the theoretical value required to reach the desired SNR, as the latter is only limited by Poisson photons statistics. Fig. 1i compares DQE *vs. D* values for a commercial direct conversion detector (amorphous Se, data from Ref.[21]) and scintillator (GOS, obtained *via* SNR analysis of images), and MAPbI$_3$ SC operated in XPV mode [calculated according to Eq. (1), using herein measured NED=90 pGy$_{air}$ and DE=88%]. The DQE values for MAPbI$_3$ SC were further confirmed by SNR analysis of X-ray images at the doses of 8 nGy$_{air}$ and 32 nGy$_{air}$ (Fig. 1g, h; see details in the **Methods section**). Noteworthy, a dose of 8 nGy$_{air}$ is *ca.* three orders in magnitude lower than the one received by the patient during typical X-ray imaging[44] or those typically used for X-ray imaging with perovskites[13,25]. With NED being smaller than one photon, the noise levels need not to be further improved for minimization of the accumulated dose for achieving the same X-ray imaging quality. In the following, we further detail the rationale and the experimental path to attain such characteristics of the MAPbI$_3$ SC detector.

Detection efficiency and charge transport properties of MAPbI$_3$ SC. The highest DE-values are expected in the SC thickness range 50-150 μm, where the experimental CCE and AE, computed from database values[45], are both high (Extended Data Fig. 2). For the simplest case, that is a single kind of charge carriers originating from the absorption of photons by the device surface, CCE can be expressed with the Hecht equation[46]:

$$\text{CCE} = \frac{L_d}{d}\left(1 - \exp\left(-\frac{d}{L_d}\right)\right) \tag{2}$$

where d is the drift distance (equal to the device thickness) of a charge to the corresponding electrode, $L_d = \mu\tau E$ is the charge carrier drift length, E is the electrical field, $E=U/d$ with U is the electrical potential. Kabir and Kasap[47] developed a model for CCE (and DE) under X-ray exposure, where the Hecht equation is modified to account for the penetration depth of X-rays and hence a volumetric distribution of generated charges, as well as asymmetry of transport properties for electrons and holes. We first use this model to assess the expected performances of XPV devices with given charge transport properties and in relation to the SC thickness and then compare to the experimental CCE and DE values. For the XPV mode, the electrical field strength E is fully defined by build-in
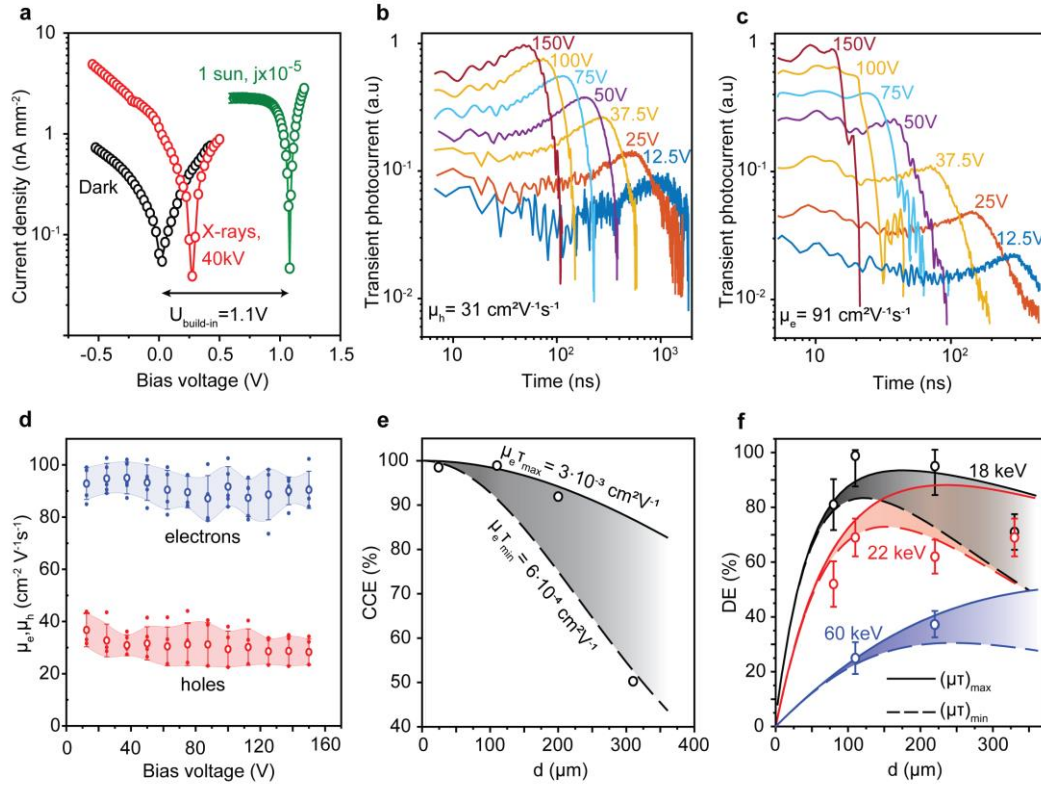
Fig. 2 | CCE and DE of MAPbI₃ SC XPV detectors. a, I-V curves in the dark and under X-ray and light illumination, used to estimate the build-in potential of *ca.* 1.1V. **b, c**, Time-of-flight traces for holes (b) and electrons (c) under blue laser pulses for various bias voltages, used to determine the charge carrier mobility. **d**, Mobility dependence on bias voltage for electrons (blue) and holes (red). Solid points show experimental data; open circles show data averaged for corresponding bias voltage, shaded area points on the standard deviation of mean values. **e**, Calculated CCE dependence on MAPbI₃ SC thickness based on the Hecht equation with drift length estimated from experimental data with lower (dashed line) and upper (solid line) limit of a lifetime. Circles represent CCE experimental data for illumination with optical photons. **f**, X-ray DE dependence on thickness for different X-ray photon energies (shown in different colors), calculated based on model (lines) with upper (solid) and lower (dashed) limits of $\mu\tau$ evaluation. Open circles represent the experimental DE data.

potential U, *i.e.* open-circuit voltage V_{oc}=1.1 V under one-sun illumination conditions. (Fig. 2a), which was additionally confirmed with the photocurrent dependence on the bias voltage under X-ray irradiation (Extended Data Fig. 3a). Estimation of $\mu\tau$ values are, however, somewhat ambiguous. Their lower limit ($\mu_e\tau_{min}$= 6·10⁻⁴ cm²V⁻¹ and $\mu_h\tau_{min}$= 2·10⁻⁴ cm²V⁻¹) was estimated by separately measuring the mobility of each carrier type using the time-of-flight technique[48] (Fig. 2b-d) and multiplying these values by their mean lifetime estimated from the transient photocurrent response (τ≥6 μs; Supplementary Fig. 3). The upper $\mu\tau$ limit for the majority carrier ($\mu_e\tau_{max}$= 3·10⁻³ cm²V⁻¹) was directly obtained as a fitting parameter (in the Hecht equation) of photocurrent *vs.* bias voltage dependence (Extended Data Fig. 3b). For devices illuminated from the side of the hole-collecting electrode, $\mu_e\tau$

8

values set the CCE dependency on the detector thickness, being in good agreement with the experiment (Fig. 2e).

Then the thickness-dependent DE is calculated for both limits, combining photon-energy-dependent AE and CCE, and accounting for ambipolar charge transport. For $\mu_h\tau_{max}$ we take a value of 30% of the $\mu_e\tau_{max}$, considering μ_e/μ_h-ratio measured by time-of-flight. Calculated DE values are in good agreement with experimental data (Fig. 2f). In particular, the DE of the 110 µm-thick device is mostly limited by AE, and reaches 88% for 18 keV X-ray radiation, while at the thicknesses larger than 200 µm, the DE becomes limited by CCE.
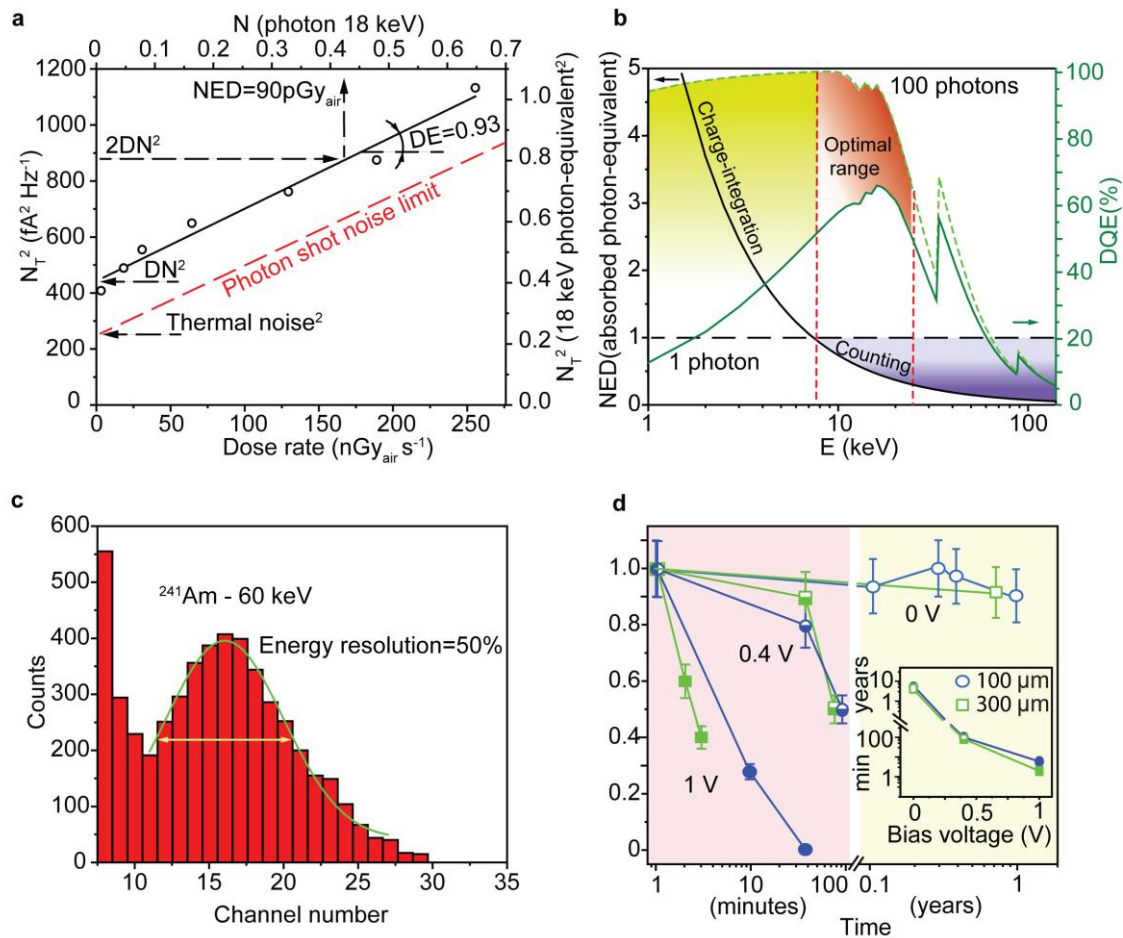

Fig. 3 | X- and γ-ray detection performance for MAPbI₃ SC XPV device. a, Squared noise current spectral density dependence on dose rate together with N_T squared, expressed in photon-equivalents, depending on mean photon number over integration time 500 µs (black circles are experimental data, the black line is fit with Eq. (3). **b**, NED (black line) and DQE (green lines) *vs.* photon energy, calculated from the experimental DE and NED; DQE is shown for single (solid line) and 100 photons (dashed line); the energy ranges where are only the charge-integration regime is possible and photon counting regime becomes allowed are highlighted, respectively, in yellow and blue. The optimal energy range is shaded in red. **c**, Energy resolved spectrum of 60 keV photons from a radioactive ²⁴¹Am source. **e,** Normalised SNR dependence *vs.* time for various bias voltage and device thickness. Inset shows estimated half-life (time corresponds to 50% drop of normalized SNR) dependence on the bias voltage.

Detection performance for MAPbI$_3$ SC XPV device. Whereas DE sufficiently describes the detector signal, NED is the comprehensive descriptor for the noise of the detector. To estimate NED, the X-ray dose-rate-dependent total noise (N$_T$) of MAPbI$_3$ SC detector was obtained as the noise current spectral density (Fig. 3a, Extended Data Fig. 4). N$_T^2$ is also expressed in photon-equivalents units, where a single photon-equivalent is the root-mean-square (RMS) of the noise-charge equal to the charge generated by one photon in the time window t (equal to 500 µs, given by the amplifier bandwidth 1 kHz; see the additional Y-axis on the right of Fig. 3a). In Fig. 3a the dose rate is recalculated to an equivalent photon quantity within t. The dependence of N$_T^2$ *vs.* n_{ph} is a linear function with a slope of DE and an offset of DN^2 (details in Supplement Note 2):

$$N_T^2[photon-equivalent^2]=DE \cdot n_{ph}+DN^2 \qquad (3)$$

The red line on Fig. 3a shows the theoretical limit for a sum of photon shot and thermal noises. A fit of experimental data with Eq. (3) gives DE=0.93, in good agreement with the DE estimated from CCE and AE (Fig. 2f). The experimental DN exceeds by just ~30% the fundamental lowest limit given by the thermal noise[49], calculated based on device resistance. Such low DN emphasizes the absence of dark-current-induced electron shot noise and insignificance of the effects of ionic diffusivity in the XPV mode. NED was then calculated as the offset/slop ratio in the Eq. (3) according to Eq. (S19.2)[43] and amounted to ~0.4 photon-equivalents at 18 keV, which corresponds to a dose of *ca.* 90 pGy$_{air}$ at 0.8 mm^2 detector area.

Single-photon detection capability stems directly from the NED being below one photon-equivalent; see examples of obtained single-photon signal traces with different types of pre-amplifiers in Extended Data Fig. 5, Supplementary Fig. 4. NED *vs.* X-ray energy plot allows estimating the energy onset for the photon-counting regime (for instance, *ca.* 7 keV for a 110 µm-thick device, Fig. 3b), as opposed to charge-integration mode used for lower energy photons (with higher flux). On the other hand, DQE begins to decline with further increase in photon energies as the AE drops (see Supplementary Note 4 for details of calculation NED and DQE dependence on energy), defining the range of *ca.* 10-25 keV (110 µm-device) for near-to-ideal detector performance, optimal for X-ray imaging at low doses and which is limited mostly by the photon shot noise (Fig. 1g, h). In this energy range, the DQE reaches 90% upon absorption of just a dozen of photons by the device (within t, Extended Data Fig. 6). Low-noise and high charge collection characteristics allow single-photon counting from a ^{241}Am source (60 keV) with an energy resolution of *ca.* 50% (Fig. 3c).

Owing to zero-bias operation, these XPV devices retain their characteristics for at least one year (in air, without encapsulation), with the projected device half-life (defined as 50% drop of normalized SNR) of several years, whereas complete degradation occurs within a few hours at high applied electric fields (Fig. 3d). The

operational stability of XPV devices thus reaches the typical chemical shelf-life of MAPbI$_3$ SC, despite the relatively high dose accumulated during these tests (equivalent to ca. 500 conventional X-ray medical scans; see Supplementary Fig. 5).
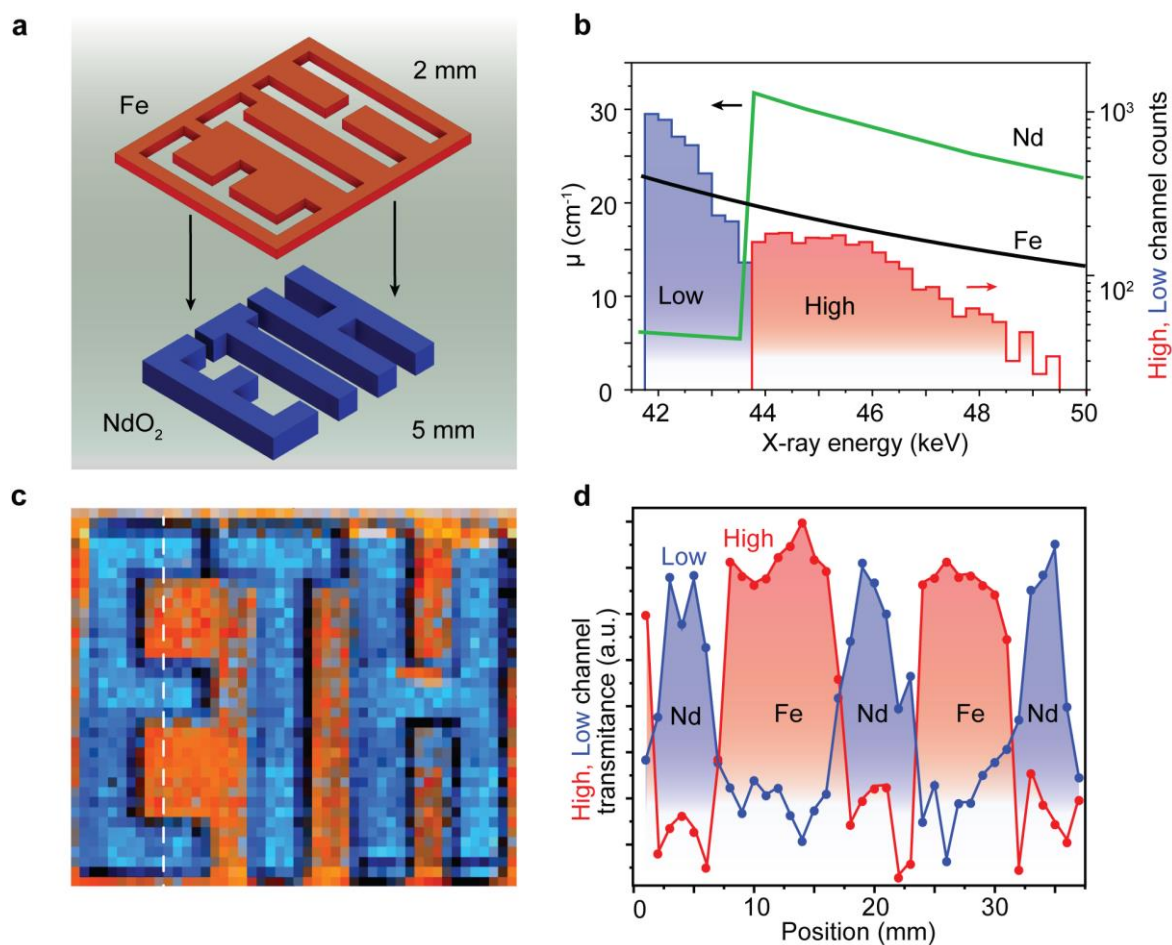

Fig. 4 | X-ray energy-resolved imaging. a, Imaged object is a rectangle comprising two complementary patterns - 5 mm thick ETH letters made of NdO$_2$ powder surrounded by the 2 mm thick steel frame. **b**, Attenuation coefficients *vs.* X-ray photon energy for Fe (black curve) and NdO$_2$ (green curve) shown on top of an example of 50 kV$_p$ energy spectrum transmitted through the Nd part of the object recorded by MAPbI$_3$ SC detector. Spectrum was binned into low (blue) and high (red) channels, with a border that corresponds characteristic *K*-line of Nd. **c,** Energy resolved X-ray imaging of the object from (**a**) under 50 kV$_p$ X-ray with MAPbI$_3$ SC detector, where the colors decode transmittance for corresponding 2 energy channels from (**b**). **d,** Transmittance of low (blue) and high (red) channels along white dashed line on (**c**).

X-ray energy-resolved imaging. While the obtained energy resolution is not suitable for applications in high-resolution γ-spectroscopy, it fully suffices for energy-discriminated X-ray spectral imaging, so-called "X-ray multicolor imaging"[50]. As a showcase, we used a several-mm-thick rectangular object consisting of two complementary "ETH" patterns made of two different materials with different X-ray attenuation vs. X-ray energy dependencies (Fe and NdO$_2$, Fig. 4a). Specifically, compared to Fe, the X-ray attenuation coefficient of Nd is

much lower below 43 keV and much higher above this value (due to its *K*-atomic shell, Fig. 4b). The thicknesses of each pattern were adjusted for attaining minimal overall X-ray transmission contrast; the letters are then somewhat readable only due to X-ray shadowing when imaging at a non-orthogonal angle to the X-ray tube (Supplementary Fig. 6). One can readily distinguish between two materials and obtain a high-contrast image when recording the images using low-energy channel (more attenuated by Fe) or high-energy channel (more suppressed by Nd), seen as red and blue regions, respectively (Fig. 4c-d).

In conclusion, $MAPbI_3$ SC X-ray detectors operated in the photovoltaic mode are shown to exhibit long-term stable and near-to-ideal performance in the soft X-ray range (18-25 keV), with DQE~87% at a low dose of 8 nGy_{air}, NED~90 $pGy_{air,}$ and DE up to 88%. These findings attest the suitability of hybrid lead halide perovskites – when operated in the photovoltaic mode – as a practical low-cost detector technology for medical X-ray imaging such as mammography, where high SNR at a low dose is crucial, and hence motivate future work on the development of commercial perovskite-based XPV array detectors.

References:

1. Locker, M. *et al.* Single photon counting X-ray imaging with Si and CdTe single chip pixel detectors and multichip pixel modules. *IEEE Trans. Nucl. Sci.* **51**, 1717-1723 (2004).
2. Brombal, L. *et al.* Large-area single-photon-counting CdTe detector for synchrotron radiation computed tomography: a dedicated pre-processing procedure. *J. Synchrotron Radiat.* **25**, 1068-1077 (2018).
3. Yakunin, S. *et al.* Detection of X-ray photons by solution-processed lead halide perovskites. *Nat. Photonics* **9**, 444-449 (2015).
4. Zhou, Y., Chen, J., Bakr, O. M. & Mohammed, O. F. Metal halide perovskites for X-ray imaging scintillators and detectors. *ACS Energy Lett.* **6**, 739-768 (2021).
5. Sytnyk, M., Deumel, S., Tedde, S. F., Matt, G. J. & Heiss, W. A perspective on the bright future of metal halide perovskites for X-ray detection. *Appl. Phys. Lett.* **115**, 190501 (2019).
6. Yakunin, S. *et al.* Detection of gamma photons using solution-grown single crystals of hybrid lead halide perovskites. *Nat. Photonics* **10**, 585-589 (2016).
7. He, Y. *et al.* Resolving the Energy of γ-Ray Photons with MAPbI3 Single Crystals. *ACS Photonics* **5**, 4132-4138 (2018).
8. Hui, Y. *et al.* Stability of Perovskite Thin Films under Working Condition: Bias-Dependent Degradation and Grain Boundary Effects. *Adv. Funct. Mater.* **31**, 2103894 (2021).
9. Futscher, M. H. *et al.* Quantification of ion migration in $CH_3NH_3PbI_3$ perovskite solar cells by transient capacitance measurements. *Mater. Horiz.* **6**, 1497-1503 (2019).
10. Khenkin, M. V., K M, A., Katz, E. A. & Visoly-Fisher, I. Bias-dependent degradation of various solar cells: lessons for stability of perovskite photovoltaics. *Energy Environ. Sci.* **12**, 550-558 (2019).
11. Domanski, K. *et al.* Not All That Glitters Is Gold: Metal-Migration-Induced Degradation in Perovskite Solar Cells. *ACS Nano* **10**, 6306-6314 (2016).
12. Liu, Y. *et al.* Ligand assisted growth of perovskite single crystals with low defect density. *Nat. Commun.* **12**, 1686 (2021).
13. Kim, Y. C. *et al.* Printable organometallic perovskite enables large-area, low-dose X-ray imaging. *Nature* **550**, 87-91 (2017).
14. Milbrath, B. D., Peurrung, A. J., Bliss, M. & Weber, W. J. Radiation detector materials: An overview. *J. Mater. Res.* **23**, 2561-2581 (2008).
15. Wang, P. L. *et al.* Hard Radiation Detection from the Selenophosphate Pb2P2Se6. *Adv. Funct. Mater.* **25**, 4874-4881 (2015).
16. Stoumpos, C. C. *et al.* Crystal growth of the perovskite semiconductor $CsPbBr_3$: a new material for high-energy radiation detection. *Cryst. Growth Des.* **13**, 2722-2727 (2013).
17. Androulakis, J. *et al.* Dimensional Reduction: A Design Tool for New Radiation Detection Materials. *Adv. Mater.* **23**, 4163-4167 (2011).
18. Abbaspour, S., Mahmoudian, B. & Islamian, J. Cadmium telluride semiconductor detector for improved spatial and energy resolution radioisotopic imaging. *World J. Nucl. Med.* **16**, 101-107 (2017).
19. Fiederle, M., Procz, S., Hamann, E., Fauler, A. & Fröjdh, C. Overview of GaAs und CdTe pixel detectors using Medipix electronics. *Cryst. Res. Technol.* **55**, 2000021 (2020).
20. Pan, W. *et al.* $Cs_2AgBiBr_6$ single-crystal X-ray detectors with a low detection limit. *Nat. Photonics* **11**, 726-732 (2017).
21. Panneerselvam, D. M. & Kabir, M. Z. Evaluation of organic perovskite photoconductors for direct conversion X-ray imaging detectors. *J. Mater. Sci.: Mater. Electron.* **28**, 7083-7090 (2017).
22. Shrestha, S. *et al.* High-performance direct conversion X-ray detectors based on sintered hybrid lead triiodide perovskite wafers. *Nat. Photonics* **11**, 436-440 (2017).
23. Matt, G. J. *et al.* Sensitive direct converting X-Ray detectors utilizing crystalline $CsPbBr_3$ perovskite films fabricated via scalable melt processing. *Adv. Mater. Interfaces* **7**, 1901575 (2020).
24. Tie, S. *et al.* Robust fabrication of hybrid lead-free perovskite pellets for stable X-ray detectors with low detection limit. *Adv. Mater.* **32**, 2001981 (2020).
25. Zhao, J. *et al.* Perovskite-filled membranes for flexible and large-area direct-conversion X-ray detector arrays. *Nat. Photonics* **14**, 612-617 (2020).
26. He, Y. *et al.* $CsPbBr_3$ perovskite detectors with 1.4% energy resolution for high-energy γ-rays. *Nat. Photonics* **15**, 36-42 (2021).
27. Deumel, S. *et al.* High-sensitivity high-resolution X-ray imaging with soft-sintered metal halide perovskites. *Nat. Electron.* **4**, 681-688 (2021).
28. Wei, H. *et al.* Dopant compensation in alloyed CH3NH3PbBr3−xClx perovskite single crystals for gamma-ray spectroscopy. *Nat. Mater.* **16**, 826-833 (2017).
29. He, Y. *et al.* Demonstration of Energy-Resolved γ-Ray Detection at Room Temperature by the CsPbCl3 Perovskite Semiconductor. *J. Am. Chem. Soc.* **143**, 2068-2077 (2021).

30. Jeong, J. *et al.* Pseudo-halide anion engineering for α-FAPbI3 perovskite solar cells. *Nature* **592**, 381-385 (2021).

31. Datta, A., Zhong, Z. & Motakef, S. A new generation of direct X-ray detectors for medical and synchrotron imaging applications. *Sci. Rep.* **10**, 20097 (2020).

32. Peng, J. *et al.* X-ray detection based on crushed perovskite crystal/polymer composites. *Sens. Actuator A Phys.* **312**, 112132 (2020).

33. Chen, Z. *et al.* Single-Crystal MAPbI$_3$ Perovskite Solar Cells Exceeding 21% Power Conversion Efficiency. *ACS Energy Lett.* **4**, 1258-1259 (2019).

34. Alsalloum, A. Y. *et al.* Low-Temperature Crystallization Enables 21.9% Efficient Single-Crystal MAPbI$_3$ Inverted Perovskite Solar Cells. *ACS Energy Lett.* **5**, 657-662 (2020).

35. Alsalloum, A. Y. *et al.* 22.8%-Efficient single-crystal mixed-cation inverted perovskite solar cells with a near-optimal bandgap. *Energy Environ. Sci.* **14**, 2263-2268 (2021).

36. Saidaminov, M. I. *et al.* High-quality bulk hybrid perovskite single crystals within minutes by inverse temperature crystallization. *Nat. Commun.* **6**, 7586 (2015).

37. Fateev, S. A. *et al.* Solution Processing of Methylammonium Lead Iodide Perovskite from γ-Butyrolactone: Crystallization Mediated by Solvation Equilibrium. *Chem. Mater.* **30**, 5237-5244 (2018).

38. Tress, W. Metal Halide Perovskites as Mixed Electronic–Ionic Conductors: Challenges and Opportunities—From Hysteresis to Memristivity. *J. Phys. Chem. Lett.* **8**, 3106-3114 (2017).

39. Neamen, D. A. *Semiconductor Physics and Devices: Basic Principles 4th ed.*, 633-635 (McGraw-Hill, New York, 2012).

40. Pan, L., Shrestha, S., Taylor, N., Nie, W. & Cao, L. R. Determination of X-ray detection limit and applications in perovskite X-ray detectors. *Nat. Commun.* **12**, 5258 (2021).

41. Berger, M., Yang, Q. & Maier, A. *Medical Imaging Systems*. 136-139 (Springer International Publishing, Cham, 2018).

42. Zanella, G. & Zannoni, R. The role of the quantum efficiency on the DQE of an imaging detector. *Nucl. Instrum. Methods Phys. Res. A* **381**, 157-160 (1996).

43. Isaias, D. J., Sarah, J. B., Michael, J. P. & Kungang, Z. A comparison of quantum limited dose and noise equivalent dose.in *SPIE Medical Imaging 2016 - Proceedings.*

44. Mettler, F. A., Huda, W., Yoshizumi, T. T. & Mahesh, M. Effective Doses in Radiology and Diagnostic Nuclear Medicine: A Catalog. *Radiology* **248**, 254-263 (2008).

45. Berger, M. J. *et al. XCOM: Photon Cross Sections Database*; https://www.nist.gov/pml/xcom-photon-cross-sections-database (2013).

46. Cho, H. Y., Lee, J. H., Kwon, Y. K., Moon, J. Y. & Lee, C. S. Measurement of the drift mobilities and the mobility-lifetime products of charge carriers in a CdZnTe crystal by using a transient pulse technique. *J. Instrum.* **6**, C01025 (2011).

47. Zahangir Kabir, M. & Kasap, S. O. Sensitivity of x-ray photoconductors: Charge trapping and absorption-limited universal sensitivity curves. *J. Vac. Sci. Technol.* **20**, 1082-1086 (2002).

48. Shrestha, S. *et al.* Assessing temperature dependence of drift mobility in methylammonium lead iodide perovskite single crystals. *J. Phys. Chem. C* **122**, 5935-5939 (2018).

49. Johnson, J. B. Thermal agitation of electricity in conductors. *Phys. Rev.* **32**, 97-109 (1928).

50. Moghiseh, M. *et al.* Discrimination of multiple high-Z materials by multi-energy spectral CT– a phantom study. *JSM Biomed. Imaging Data Pap.* **3**, 1007 (2016).

Author contributions.

 K.S. measured X-ray and noise performance, formulated detector figure-of-merit requirements, made X-ray imaging experiments, analyzed the results with a contribution of G.M and S.Y.; G.M. K.S. and S.Y. measured charge transport characteristics; B.T. and M.N.L. developed MAPbI$_3$ SCs growth, fabricated XPV devices, characterized them under 1-sun illumination, and measured external quantum efficiency. M.N.L. performed scanning electron microscopy B.T. and R.N. fabricated device for ToF measurement. K.S., S.Y. and M.V.K. wrote the manuscript with the contribution of all co-authors. M.V.K., S.Y., O.F.M., and O.M.B. supervised the work. K.S. and B.T. contributed equally to this work. All authors discussed the results and commented on the manuscript.

Competing financial interests: The authors declare no competing financial interest.

Additional Information

Supplementary Information is available for this paper.

Materials & Correspondence Maksym V. Kovalenko (mvkovalenko@ethz.ch)

Correspondence and requests for materials should be addressed to M.V.K.

Methods

Reagents. γ-Butyrolactone (GBL, >99%), toluene (anhydrous, 99.8%), fullerene (C_{60}, 98%) bathocuproine (BCP, 99.99%) and Octadecyltricholorosilane (OTS) were purchased from Sigma Aldrich. Methylammonium iodide (MAI) was purchased from Greatcell Solar Limited. Lead (II) iodide (PbI_2, ultradry beads, 99.999%) was purchased from Alfa Aesar. Poly(triarylamine) (PTAA, >99%, Sublimed) was purchased from Xi'an Polymer Light Technology Corp. All reagents were used as received.

Preparation of substrates for SC growth. ITO substrates with the area of 5×5 cm^2 (8-15 Ω, Delta Technologies LTD,) were cleaned by sonication in soap, deionized water, acetone, and isopropanol sequentially, followed by UV-ozone surface treatment for 10 minutes. Next, the PTAA solution (2.5 mg/ml in toluene) was spin-coated for 30 s at 4000 rpm, and subsequently annealed at 100 °C for 10 min.

Growth of MAPbI$_3$ SC. The crystal growth is modified from the previous reports[33,34]. Briefly, 1.55 M of MAI and PbI_2 were dissolved in GBL at 60 °C by stirring overnight. 50-750 µl of the solution was placed on a prepared substrate with a spacer (thickness of 20-300 µm) preheated to the solution temperature and enclosed by another PTAA-coated substrate. To induce nucleation and to promote growth, the hotplate was gradually heated to 130 ⁰C with a rate of 2 ⁰C/h. After the crystallization was finished, the substrates were separated and the remnant solution was quickly cleaned with Kimwipes. Substrates were allowed to cool slowly to room temperature on the hotplate to ensure good electrical and mechanical contact between the substrate and thin SCs. All procedures other than substrate cleaning were carried out in a nitrogen atmosphere.

Device Fabrication. C_{60} (20 nm) and BCP (3 nm) were thermally evaporated without an evaporation mask at a rate of 0.1 Å/s on top of the crystals. Then, Kapton tapes were used to form an evaporation mask for Cu electrode (thickness of 80 nm) on the edge of the SCs to avoid short-circuiting. When it isn't mentioned specifically, all further described measurements were conducted with MAPbI$_3$ SC XPV devices with the electrode structure given in Fig. 1c.

Device Fabrication for ToF measurement. First, ITO substrates were first treated with Octadecyltricholorosilane (OTS) base self-assembled monolayer (SAM) and ensured that the surface is insulating and hydrophobic. 1mM OTS solution bath in isopropanol (IPA) was prepared and the ITO substrates were dipped inside for the 10 minutes. Later the substrates were washed with fresh IPA to remove the excess of absorbed OTS. The perovskite single crystals were grown on the SAM treated substrates using the same crystallization technique to fabricate XPV devices. After crystal growth, the devices are completed with Cu evaporation.

Charge collection efficiency. CCE was estimated to be equivalent to IQE (considering the corresponding travel distance of charge carriers), measured using a QEX10 Spectral Response Measurement System (PV Measurements, Inc.), calibrated against a reference silicon photodiode.

Scanning electron microscope (SEM) images were taken under a Teneo VS SEM (Thermo Fisher Scientific). The thicknesses of the crystals were measured by using a profilometer (KLA-Tencor P-7 Stylus).

Time of flight (ToF) method was used for the measurement of the drift velocity of photo-excited charge carriers under an applied electric field. The ToF experiment was performed in the differential mode, where the total number of photo-excited charge carriers is kept sufficiently below the total charge on the electrodes of SC and the RC time constant of the ToF apparatus is below the transit time of the charge carriers. The photo-excitation is applied through the ITO glass substrate with a diode laser from Becker & Hickl (model BDL-488-SMN wavelength of 488 nm, pulse duration of about 40 ps,). To prevent a field-induced polarization (*i.e.* accumulation of ions at the electrodes), the bias is applied as a pulse train of alternating polarity from ±20 to ±150V with a frequency of 150 Hz from HP 8116A function generator *via* FS WMA-300 high voltage amplifier. The drift-time τ is inversely proportional to the drift mobility μ and is given by $\mu = d^2/(\tau V)$. Where d is the drift distance, τ is the drift-time and V is the applied bias.

Photoresponse. For evaluating the mobility–lifetime product, $\mu\tau$, a current *vs.* voltage measurement was obtained with the symmetrical (both contacts are Cu) laterally-contacted $MAPbI_3$ SC under modulated light from LED with a wavelength of 450 nm. The sample was biased by Keithley 236 SMU, while the photoinduced current was restored by lock-in amplifier SR830 from Stanford Research.

Lifetime measurements with transient photocurrent. Transient photocurrent lifetime measurements were made with the symmetrical (both contacts are Cu) laterally-contacted $MAPbI_3$ SC under the pulsed (20-100 µs long, the wavelength of 450 nm) LED illumination. The lifetime was extracted from the exponential fit of the signal decay[51].

X-ray characterization. X-ray attenuation is calculated based on the open NIST database[45]. All X-ray irradiation experiments were done utilizing the X-ray tube from Amptek (model Mini-X, with Ag target). The radiation dose rate measurements are performed with a PM1621A dosimeter from Polimaster. Sensitivity measurements (Fig. 1d) for $MAPbI_3$ and CdZnTe SCs are carried out with Keithley 236 SMU under X-ray irradiation with $40kV_p$. For AC bias measurements, the symmetrical laterally-contacted $MAPbI_3$ SC with Cu was used. The function generator HP 8116A with the AC voltage amplifier FS WMA-300 was utilized for biasing, $40kV_p$ X-ray was modulated with a lead chopper wheel, the signal was restored on lock-in amplifier SR860 from Stanford Research. SNR,

detection limit, noise, and stability measurements (Fig. 1e,f, Fig. 3a,d) were obtained with samples connected *via* the low-noise current amplifier Femto DLPCA-200 to the spectral network analyzer SR770 from Stanford Research with irradiation by modulated 20 kV_p X-ray irradiation, attenuated by a 3 mm glass filter. The noise current spectral density dependence on the dose rate (Fig. 3a) was measured at the frequency of 960 Hz with the 110 μm thick device with are 0.8 mm^2, resistance of 6 MΩ. Experimental DQE values on Fig. 1i were calculated according to $DQE = SNR_{detector}^2/SNR_{ideal}^2$, where $SNR_{detector}$ was calculated as the ratio of the average count number at certain X-ray photon flux to the corresponding counts RMS, while SNR_{ideal} was taken as $\sqrt{n_{ph}}$, where the photon number n_{ph} was evaluated based on the count rate of a reference CdZnTe SC detector. Sensitivity values for DE evaluation on Fig. 2f were estimated with modulated X-ray irradiation, the sample was connected *via* the low-noise current amplifier Femto DLPCA-200 and the signal was restored by lock-in amplifier SR860. For the photon energies of 60 keV, we obtained DE as a ratio of the measured counting rate to the calculated value expected taking into the account activity of the [241]Am source. The energy-resolved spectrum for [241]Am source (activity of 0.4 MBq) was measured with a charge-sensitive preamplifier (A250CF CoolFET from Amptek) coupled with an amplifier-shaper (Model 572 from ORTEC) and a digital multichannel analyzer (MCA-8000D from Amptek).

X-ray imaging. All images were acquired in a single-photon counting mode while an object was 2D-scanned in a lateral direction towards the detector. The image at Fig. 4c was obtained under 50kV_p X-ray filtered by 500 μm thick steel plate to cut lower energy part (the corresponding spectrum is presented in the Supplementary Fig. 7a), the accumulated dose per pixel is about 10 μGy. Images at Fig. 1g, h were made with 20kV_p X-ray irradiation filtered by 3 mm glass to get quasi-monoenergetic spectrum with mean 18 keV energy (Supplementary Fig. 7b). The detector was calibrated to get the highest contrast on reference points of the imaged object, indicating that the threshold in the energy spectrum is set near 43 keV as it is shown in Fig. 4b.

51.   Sze, S. M. *Semiconductor Devices: Physics and Technology*., 60-63 (Wiley, New York, 2002).

Data availability
The data that support the findings of this study are available from the corresponding authors upon reasonable request.
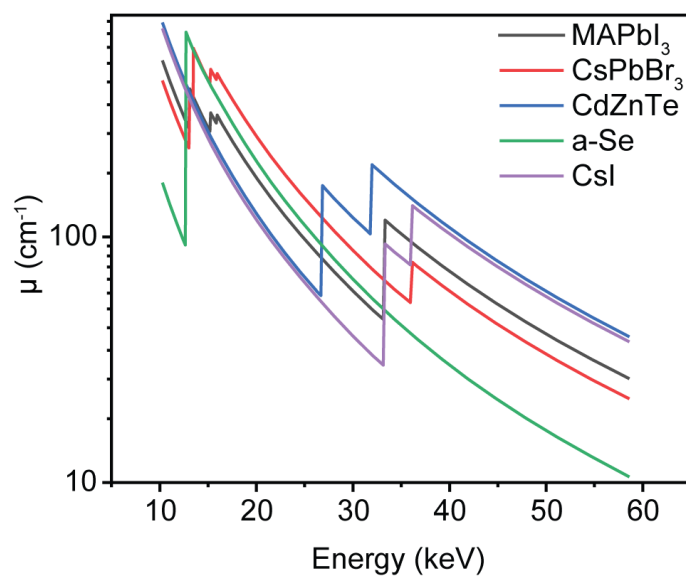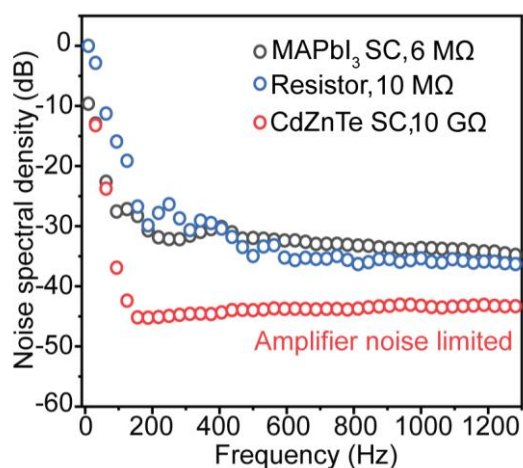
Extended Data Fig. 1 | X-ray attenuation coefficient dependence on X-ray energy. Calculated from tabulated atomic coefficients[45] for different materials typically used in the field of X-ray detection.
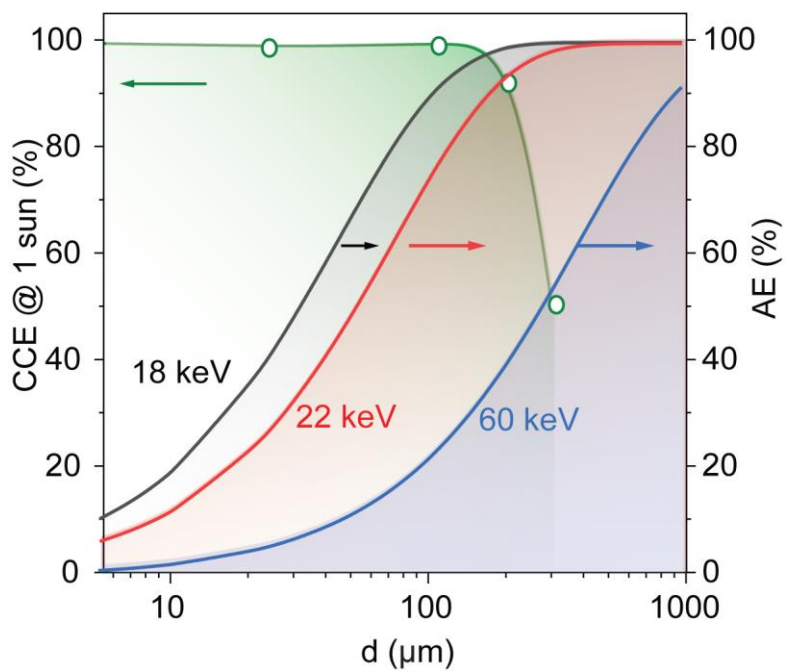
Extended Data Fig. 2 | CCE and AE thickness dependencies for MAPbI₃ SC XPV devices. CCE is evaluated for illumination with optical photons at zero-bias and AE is shown for various X-ray energies, given in different colors.
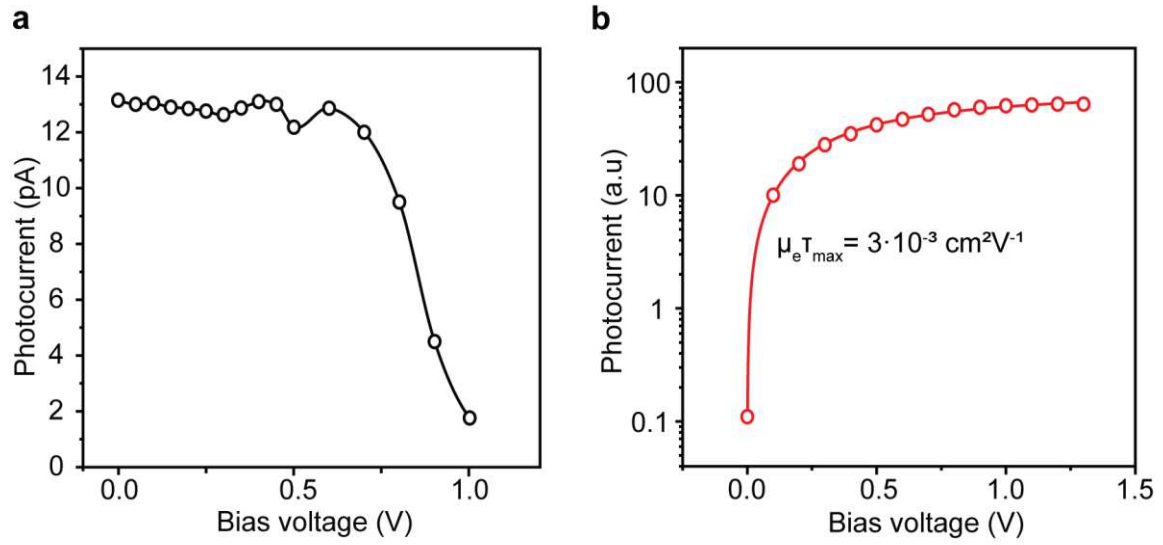
Extended Data Fig. 3 | Determination of the open-circuit voltage and µτ-product. a, Photo-induced current *vs.* bias voltage dependence for MAPbI$_3$ XPV device (thickness is 330 µm) under 50 kVp X-ray**,** open-circuit voltage V$_{OC}$ ≈ 1.05 V. **b,** Photocurrent-bias voltage dependence for asymmetrically contacted Cu/MAPbI$_3$/Cu device. Photoresponse is fitted with the Hecht equation to determine µτ.

Extended Data Fig. 4 | Thermal noise spectra. Measurements were done with the spectral analyzer SR770, and the low-noise current amplifier (Femto DLPCA-200) at $\times 10^{11}$ amplification coefficient for different test samples with no external bias voltage applied. It is seen that the noise for MAPbI$_3$ SC (of 6 MΩ internal resistance) is just slightly higher than the thermal noise for the 10 MΩ resistors. For CdZnTe SC (of 10 GΩ internal resistance), the noise is limited by the amplifier.
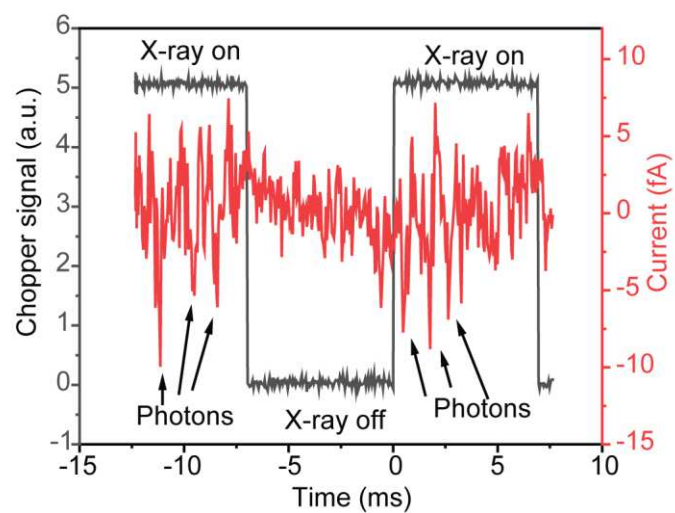
Extended Data Fig. 5 | X-ray single-photon counting. The red trace shows the modulated photocurrent measured with a low-noise current amplifier (Femto DLPCA-200) from a MAPbI$_3$ SC (thickness is 110 µm, bias is 0 V). The X-ray radiation (20 kV$_p$) was modulated by a 1.5 mm thick Pb chopper wheel. The photocurrent in the periods of open beam shows notably larger 'spikes', which are associated with single X-ray photon events.
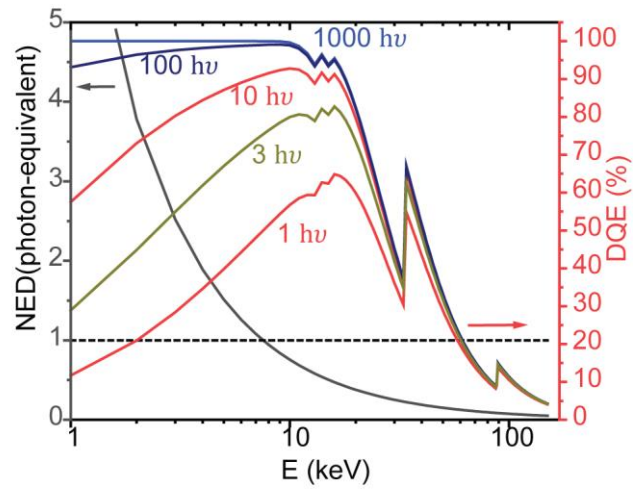
Extended Data Fig. 6 | NED and DQE dependence on X-ray photon energy and number of incident photons.
Values are calculated with Eq. S31 and Eq. S32 for MAPbI$_3$ SC (thickness is 110 µm, area of 0.8 mm^2, 0 V bias) based on experimentally measured NED and calculated AE. The dashed line shows the condition for photon counting (NED<1). The DQE is shown for different photon fluxes (*hv*, number of incident photons per integration time of 500 µs).

Supplementary Files

This is a list of supplementary files associated with this preprint. Click to download.

- StablenearidealMAPbI3XRayDetectorSUPPLEMNTARYINFO.pdf